PLOS ONE

RESEARCH ARTICLE

Design and analysis of a dual-port multiband RF-to-DC converter for IoT energy harvesting applications

Bismah Tariq[1‡*], Muhammad Amjad[1], Khaled A. Al-Jaloud[2], Waqar Ahmad Malik[3], Syed Tamoor Shah[4], Rifaqat Hussain[5*]

1 Faculty of Engineering & Technology, The Islamia University of Bahawalpur, Pakistan, **2** College of Engineering, Muzahimiyah Branch, King Saud University, P.O. Box 2454, Riyadh 11451, Saudi Arabia, **3** Department of Avionics Engineering, CAE, NUST Risalpur, Pakistan, **4** SEECS, National University of Science & Technology (NUST), Pakistan, **5** School of Electronic Engineering and Computer Science, Queen Mary University of London, United Kingdom

‡ Current Address: Faculty of Engineering & Technology, The Islamia University of Bahawalpur, Pakistan
* bismah.tariq91@gmail.com; (BT) rifaqat.hussain@qmul.ac.uk (RH)

Abstract

Internet of Things (IoT) demands efficient and sustainable energy sources for autonomous power systems. This article presents the design and analysis of a Dual-Port Multiband RF-to-DC Converter employing a multi-stage Cockcroft Walton Voltage Multiplier (CWVM) topology, which is optimized for IoT energy harvesting applications. By utilizing L-network and π-network impedance matching with distributed elements, the converter effectively harvests RF energy across six frequency bands ranging from 0.87 to 2.5 GHz. The dual-port architecture enhances power output and provides redundancy, improving the reliability of the energy harvesting system. While, the multiband feature improves the versatility of energy acquisition. The converter achieves a peak efficiency of 66% and 62% at 10 kΩ and 18 kΩ, respectively. The performance of the proposed design is comprehensively analyzed and optimized, considering the impedance matching, output voltage, and conversion efficiency. The performance of the proposed design is compared with recent converter designs in the literature, which shows that this research is a valuable contribution to the ongoing development of energy-efficient solutions. This work has significant implications for powering low-power sensors, wireless sensor networks, and other IoT devices in diverse environments, addressing the need for prolonged autonomy and reduced reliance on traditional power sources.

OPEN ACCESS

Citation: Tariq B, Amjad M, Al-Jaloud KA, Malik WA, Shah ST, Hussain R (2025) Design and analysis of a dual-port multiband RF-to-DC converter for IoT energy harvesting applications. PLoS One 20(5): e0321729. https://doi.org/10.1371/journal.pone.0321729

Editor: Suhaib Ahmed, Model Institute of Engineering and Technology, INDIA

Received: September 05, 2024

Accepted: March 11, 2025

Published: May 13, 2025

Data availability statement: All the relevant data is available within the article.

Funding: This work was supported by Researchers Supporting Project number (RSP2025R474), King Saud University, Riyadh, Saudi Arabia.

Competing interests: The authors have declared that no competing interests exist.

1 Introduction

The Internet of Things (IoT) is a transformative technology where everyday objects are inculcated with digital intelligence, enabling them to connect, communicate, and interact with each other and with humans. This interconnected web of devices and sensors, from smart thermostats to industrial machinery, has revolutionized various industries, enhancing efficiency, convenience, and data-driven decision-making [1].

However, the rapid propagation of IoT devices is accompanied by a significant challenge of surge in energy demands [2]. To overcome this challenge, Wireless power transfer (WPT) and RF energy harvesting (RFEH) [3,4], are becoming vital focus for more research now a days. These are the favorable technologies to power up wireless IoT devices [5] and ensure their continuous operation and connectivity. RFEH harnesses ambient radio frequency signals to generate electrical power, enabling sustainable and autonomous operation of IoT devices. It is useful for wireless powering of remote, hard to access, low power devices such as health care and biomedical systems [6–8], wireless sensor networks [9,10], IoT applications [11,12], and wireless communications [13].

The sources of ambient RF energy are TV/radio broadcast stations, mobile base stations, handheld stations, WiFi and Bluetooth devices, etc. [14]. As the ambient RF energy is present at different frequency bands, multiband RF-to-DC converters are desirable to combine multiple frequency bands for energy harvesting, enhancing versatility and efficiency in powering IoT devices, while reducing reliance on single-band sources and improving overall energy harvest capabilities [15].

Some single band converters are reported in the literature for energy harvesting applications [16–18]. A single band converter working at frequency band of GSM-900 with efficiency 29.85% using HSMS285C Cockcroft-Walton voltage multiplier (VM) was proposed in [16]. Another converter operating at 2.5 GHz band was proposed which has provided efficiency of 66% using HSMS2852 single stage VM [17]. A converter operating at 5G frequency band of 3.5GHz band exhibited efficiency of 42.5% using HSMS286C Greinacher VM and radial stub matching [18].

Likewise dual band converters are reported in [19–21]. In [19], the proposed dual-band converter operates on 2.1 and 2.45 GHz bands with the power conversion efficiencies of 24% and 18% respectively. The matching was achieved using multiple stubs. In [20], the proposed dual-band operates on GSM-1800 and WiFi 2.4 bands, with the conversion efficiencies of 41% and 20%, respectively. A dual-band converter was presented in [21] for GSM bands with efficiencies upto 13% at −30 dBm. The converter was implemented by single series topology and pi-matching network.

Similarly, a triple-band converter was presented in [22] with efficiency upto 42%. While a converter proposed in [23] operates on GSM-900, GSM-1800 and UMTS-2100 bands with efficiency upto 40% and output voltage of 600mV. Also some multiband converters like quad-band [24–26], six band [27] and seven band [28] are also recently reported with efficiencies ranging from 8% upto around 40% for different designs.

Some broad-band converters are also found in literature [29–31]. The converter proposed in [29] operates on 0.87–2.7 GHz band providing overall PCE of 30%. The design was implemented using voltage-doubler configuration. Two broad-band converters were proposed, operating for 1–2.4 GHz with efficiency up to 50% [30] and for 1.9–2.5 GHz with efficiency of 32% [31].

The power conversion efficiency (PCE) of an energy harvesting converter is a figure of merit for its performance evaluation [3]. Power conversion efficiency enhancement of the converter at low power levels and over a wide range of frequencies is the key challenge due to complexities involved in achievement of simultaneous impedance matching at multiple frequencies.

In this paper, a dual-port, hexa-band converter is proposed, operating on 870 MHz, 1770 MHz, 1850 MHz, 2.2 GHz, 2.41 GHz, and 2.5 GHz frequency bands. The impedance matching, output voltage and power conversion efficiency of the converter are optimized, simultaneously, on both parts of the converter. A novel configuration of multi stage Cockcroft

Walton voltage multiplier (CWVM) topology, an L-matching network and a π-matching network are used to achieve required performance. It achieves power conversion efficiencies in the range of 23 to 66% in all the desired frequency bands.

Following sections include the design technique, configuration, results, performance, discussion and the concluding remarks for the proposed converter.

2 Design technique and configuration

The RF-to-DC converter consists of four basic working blocks as shown in Fig 1. The first block is an RF input block, which is the receiving wideband or a multiband antenna in practical scenarios. Next is the impedance matching block that consists of an impedance matching network (IMN) to ensure maximum power transfer and minimized signal reflection between the RF input block and the RF-to-DC rectification/ conversion block. The last block is the DC output block, which is usually a parallel combination of output load resistor and an AC block capacitor.

Many topologies are nowadays in practice for RF-to-DC rectification purposes as stated in the literature review. However, the voltage multiplier topologies are most commonly used in RF-to-DC converters for enhanced output DC voltage levels to compensate for the battery requirements of IoT devices.

Usually, the output from single stage voltage multiplier (VM) is extremely low because the received power (energy) is low, therefore, it is desirable to duplicate each stage of the VM circuit, to get a higher DC voltage from the input RF power signal. Fot this purpose, the multistage CWVM is advantageous as its output across each stage is equal to twice the peak input AC voltage (V_p) times the number of stages (N) being used, and the output can be obtained from any number of stages depending upon the application requirement [32].

Hence the proposed scheme utilizes a 4-stage half-wave CWVM topology implemented by deploying 10 pF capacitors (C1-C8) and Schottky diode pair HSMS285C for frequency bands below 2 GHz and HSMS286C for frequency bands above 2 GHz, and shown in Fig 2. Cout is the output AC Block capacitor set as 27 pF. Schottky diode pairs are chosen because of their performance under low input power values, low voltage drop, fast switching, low saturation current, and junction capacitance. The dielectric substrate used for the design is a 0.78 mm thick sheet of Rogers 5880 with ϵ_r 2.2, $tan\sigma$ 0.0009, and a copper thickness of 0.035 mm.

2.1 Single port converters design

To achieve the dual-port converter design, initially two single-port converters are designed using lumped components as well as distributed elements. Later these two single-port rectifying branches are integrated to yield the dual-port configuration and the IMNs are tuned for the hexa-band response. Following subsections discuss the single-port and dual-port designs in detail.

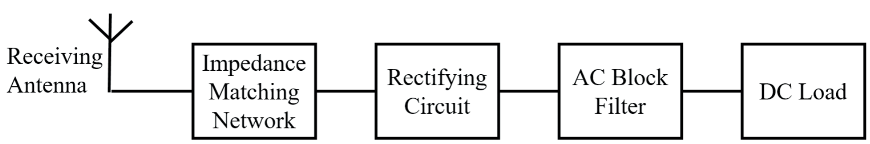

Fig 1. RF-to-DC converter block diagram.

https://doi.org/10.1371/journal.pone.0321729.g001

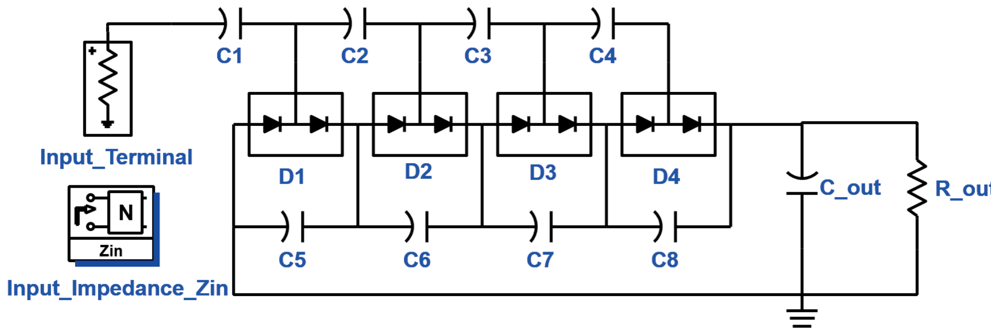

Fig 2. Schematic of 4-stage CWVM topology.

https://doi.org/10.1371/journal.pone.0321729.g002

2.1.1 Single port dual-band converter design The proposed single-port dual-band converter design is based on a single-port, single-band converter originally operating at 900 MHz. Later the modification of which yields the dual-band response for matching the converter impedance with that of the input source. An L-shape matching network, comprising the lumped components, is designed using Keysight ADS Smith chart utility. L-shape matching network is a single open stub network consisting of two reactive elements. One is the series inductive element, to provide impedance transformation and phase shift, and the other is shunt capacitive element, equivalent to the open stub. The input impedance (Z_{in}) of the converter is noted against 900 MHz as 2.653–j39.864. The lumped element values are noted as $L = 9nH$ and $C = 14.82pF$ from the Smith chart as shown in Fig 3.

After designing the lumped element networks, these are converted to distributed elements, i.e. the microstrip and transmission lines. The lengths of the transmission line sections are found from Eq (1) [33]:

$$\mathrm{Z_{in}} = Z_o \frac{Z_L + jZ_o tan\beta l}{Z_o + jZ_L tan\beta l} \tag{1}$$

where Z_{in}, Z_o, Z_L, and β are the transmission line's input impedance, the characteristic impedance, the load impedance, and the phase constant, respectively. The phase constant is calculated as Eq (2):

$$\beta = \frac{2\pi f}{v} \tag{2}$$

where f and v are the wave frequency and the speed of light in air. The input impedance Z_{inL} of an inductive element L and its corresponding transmission line section length l_1 can be calculated by Eq (3)–(5);

$$\mathrm{Z_{inL}} = jZ_o tan\beta l_1 \tag{3}$$

$$j\omega L = jZ_o tan\beta l_1 \tag{4}$$

$$L = \frac{Z_o tan\beta l_1}{\omega} \tag{5}$$

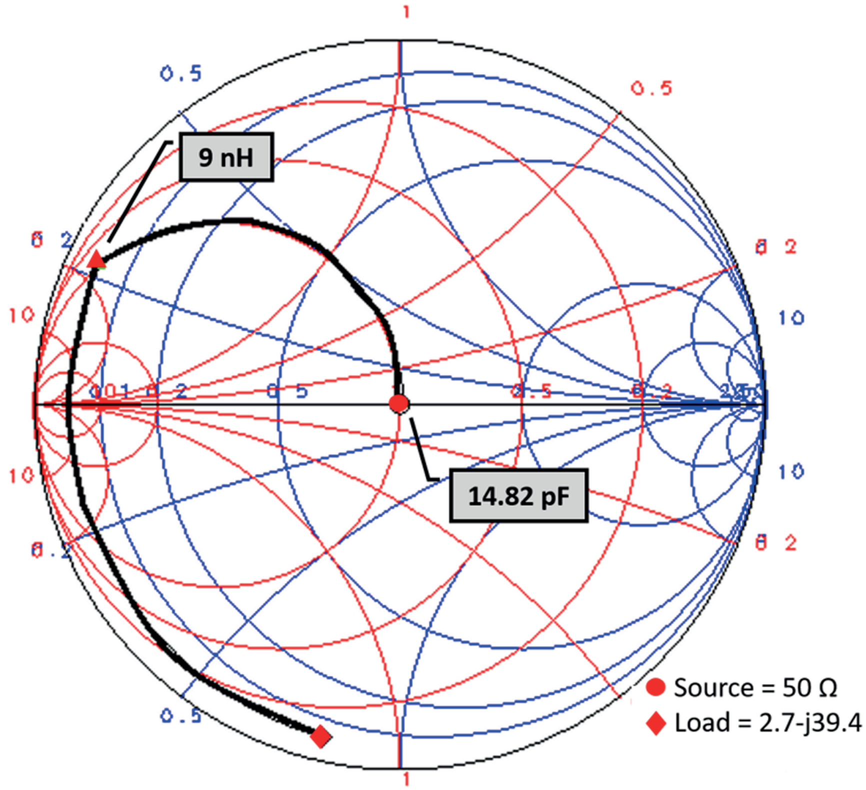

Fig 3. Impedance matching at 900 MHz using Smith chart.

https://doi.org/10.1371/journal.pone.0321729.g003

where ω is the angular frequency. On the other hand, the input impedance Z_{inC} of a capacitor, capable of capacitance C, and its corresponding transmission line's length l_2 is found by the Eq (6)–(8);

$$Z_{\mathrm{inC}} = \frac{Z_o}{jtan\beta l_2} \tag{6}$$

$$\frac{1}{j\omega C} = \frac{Z_o}{jtan\beta l_2} \tag{7}$$

$$C = \frac{jtan\beta l_2}{\omega Z_o} \tag{8}$$

Remember that the βl_1 and βl_2 obtained from the above set of equations are the electrical lengths of the transmission line sections, which are further converted to physical lengths (mm) using the LineCalc tool in ADS. To calculate the width W of the transmission line sections, Eq (9)–(12) are used [34].

$$\frac{W}{h} = \frac{2}{\pi}\left\{\left\{\frac{\epsilon_r - 1}{2\epsilon_r}\left[\ln(B-1) - \frac{0.61}{\epsilon_r} + 0.39\right] + B - 1 - \ln(2B-1)\right\}\right\},\ for\ A > 1.52 \tag{9}$$

$$\frac{W}{h} = \frac{8e^{A}}{e^{2A} - 2}, \ forA < 1.52 \tag{10}$$

$$A = \frac{Z_o}{60}\sqrt{\frac{\epsilon_r + 1}{2}} + \frac{\epsilon_r - 1}{\epsilon_r + 1}\left\{\frac{0.11}{\epsilon_r} + 0.23\right\} \tag{11}$$

$$B = \frac{529.18}{Z_o\sqrt{\epsilon_r}} \tag{12}$$

Where h is the substrate height and both A and B are variables. In our case, we found $A = 1.159$ which is <1.52. Therefore, we evaluated Eq (10) for the width of transmission line sections.

The lumped components determined from the Smith chart and the corresponding distributed elements dimensions obtained from mathematical calculations for the 900 MHz converter are listed in Table 1.

The schematics of the single port RF-to-DC converters designed using L-type matching network are shown in Fig 4.

The return loss of the 900 MHz single-port single-band converter designed with the lumped and distributed matching networks, is shown in Fig 5. It shows the converter impedance is matched in the required band.

The length of the shunt open stub achieved for 900 MHz converter is approximately $\lambda/4$. The open stub offers high impedance at its input, but its impedance becomes low when it resonates. The frequency response of an open stub is a direct function of its impedance, which is directly affected by its length. As the length increases beyond $\lambda/4$, stub introduces additional reactive behaviors that make it resonate at more than one frequencies, as more standing waves are produced. This phenomena leads to dual band response of the matching network. Adjustment of the length of the series TL section changes the overall impedance of the network, potentially shifting the resonant frequency and creating a second resonant frequency. The dimensions of the open stub and the series TL section are varied and their behavior is analyzed to achieve dual band matching at 890 and 1850 MHz. The optimized dimensions of the distributed elements of L-matching network of dual band (890 and 1850 MHz) converter, are listed in Table 2.

Note that the distributed L-type matching network require a TL section at its input (source side) for SMA connector. The return loss response of the resultant single-port dual-band converter is shown in Fig 6 which assures rectification for 890 MHz and 1850 MHz bands.

2.1.2 Single-port triple-band converter design The proposed single-port triple-band converter design is derived from the modification of a single-port, single-band converter initially operating at 2.45 GHz. To ensure impedance matching between the converter and the

Table 1. Lumped components and corresponding distributed elements dimensions (mm) for 900 MHz converter.

Lumped Components		Corresponding Distributed Elements
Parameters	**Value**	**Dimensions $w \times l$ (mm^2)**
Series Inductor L_1	9 nH	2.4 × 30.99
Shunt Capacitor C_1	14.82 pF	2.4 × 52.1
–		2.4 × 5 (Input TL Section)

https://doi.org/10.1371/journal.pone.0321729.t001

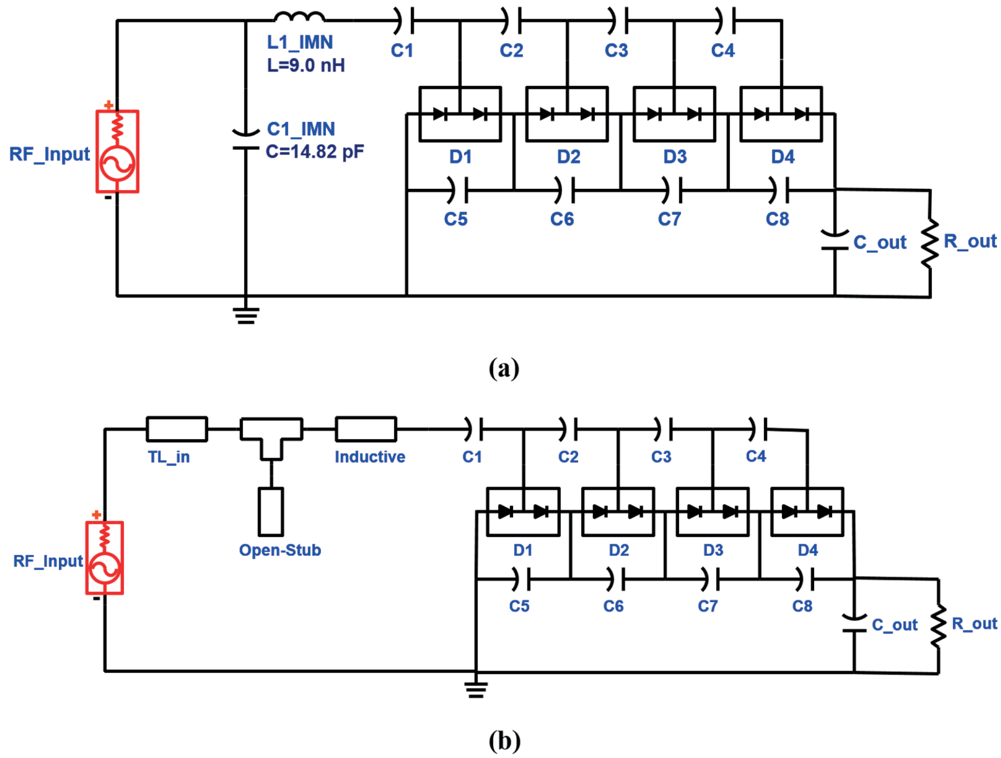

Fig 4. Schematics of RF-to-DC converters working in GSM-900 band utilizing: (a) lumped L-type IMN. (b) Distributed L-type IMN.

https://doi.org/10.1371/journal.pone.0321729.g004

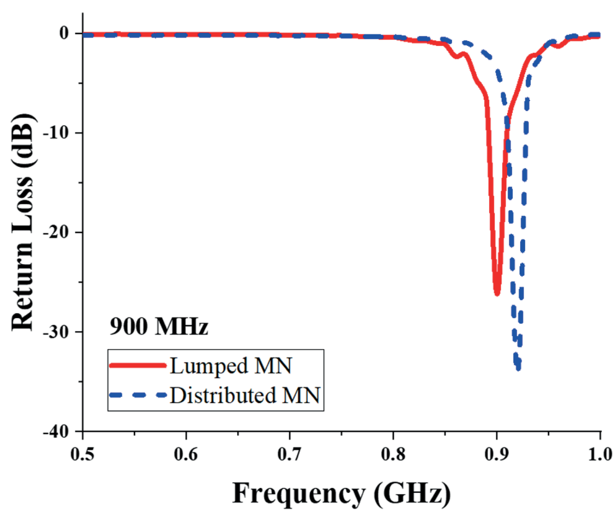

Fig 5. Return loss response of single-port single-band (900 MHz) converter.

https://doi.org/10.1371/journal.pone.0321729.g005

input source, a π-matching network, composed of lumped components, was designed using the Keysight ADS Smith Chart utility. The π-matching network is a double stub matching technique consisting of 3 reactive elements, one series inductive while two shunt capacitive (open stubs), elements. The input impedance (Zin) of the converter is noted against 2.45 GHz

Table 2. Optimized distributed elements dimensions for dual-band (890 and 1850 MHz) converter.

Parameters	Dimensions $w \times l$ (mm^2)
Series Inductive TL	2.4 × 19.31
Shunt Open Stub	3.1 × 68.67
Input TL Section	2.4 × 10

https://doi.org/10.1371/journal.pone.0321729.t002

as 54.65–j23.3. The lumped component values of the π-matching network are noted as L = 3.678nH, C_1 = 1.3139pF, and C_2 = 837.9fF from the Smith chart as shown in Fig 7.

The lumped element values hence obtained are converted to distributed elements, i.e. the microstrip transmission lines, the same way as done for 900 MHz converter design configuration earlier. The lumped components and corresponding distributed elements dimension obtained for the 2.45 GHz converter are listed in Table 3.

The schematics of the single port RF-to-DC converters designed using π-type matching network are shown in Fig 8.

The resulting return loss of the 2.45 GHz converter designed with lumped and distributed matching networks is shown in Fig 9. It shows the achievement of converter impedance matching in the required band.

Further, the dimensions of the distributed matching elements are optimized to obtain the triple band frequency response. The length of series inductive TL section is slightly increased to introduce additional phase shift and impedance transformation. The shunt open stubs are modified to a shorter lengths to introduce resonance at two additional frequencies (1.775 and 2.25 GHz), lower than 2.45 GHz. Therefore the careful optimization and analysis of the distributed elements dimensions resulted in the achievement of triple band matching response form π-matching network without introducing additional components. The optimized dimensions of the distributed elements of π-matching network of triple band (1775 MHz, 2.25 GHz, and 2.45 GHz) converter, are listed in Table 4.

Note that the distributed π-matching network requires a TL section at input (source side) for SMA connector and also at its output (load side) to be connected with rectification block

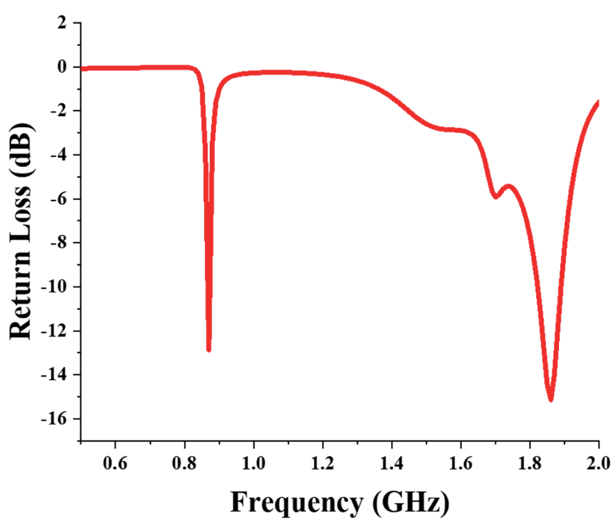

Fig 6. Return loss response of single-port dual-band (890 and 1850 MHz) converter.

https://doi.org/10.1371/journal.pone.0321729.g006

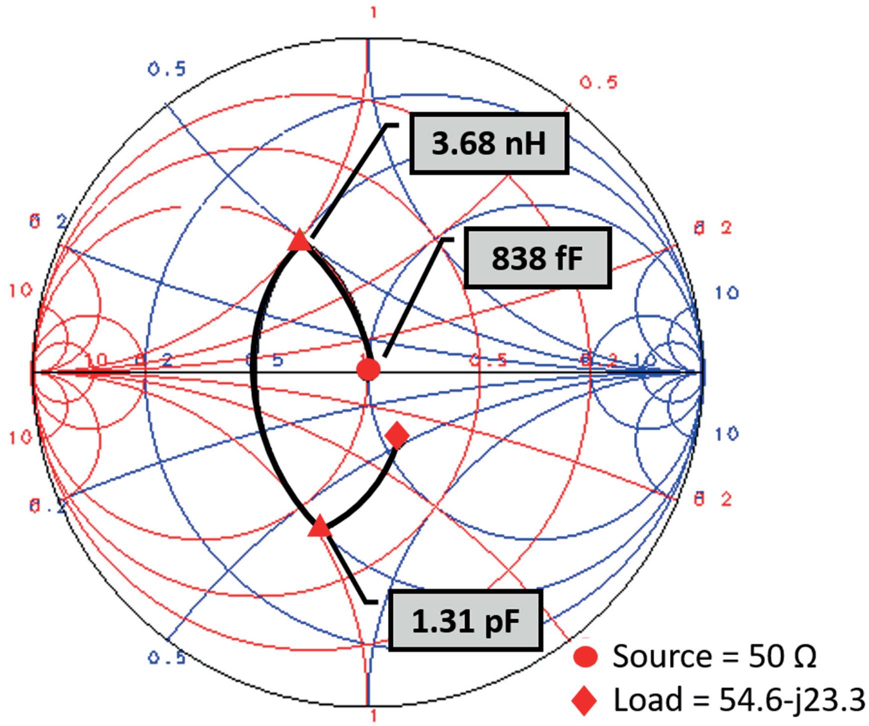

Fig 7. Impedance matching at 2.45 GHz using smith chart.

https://doi.org/10.1371/journal.pone.0321729.g007

Table 3. Lumped components and corresponding distributed elements dimensions (mm) for 2.45 GHz converter.

Lumped components		**Corresponding distributed elements**
Parameters	**Value**	**Dimensions** $w \times l$ **(mm^2)**
Series inductor L_1	3.68 nH	2.44×12.67
Shunt capacitor C_1	1.13 pF	2.44×14.21
Shunt capacitor C_2	838 fF	2.44×22.2
–		2.44×7 (input TL section)
–		2.44×0.1 (output TL section)

https://doi.org/10.1371/journal.pone.0321729.t003

elements. The triple band converter return loss is shown in Fig 10. It shows that the triple-band converter is capable to provide rectification for the 1775 MHz, 2.25 GHz, and 2.45 GHz bands.

The subsequent milestone involves the derivation of a dual-port hexa-band converter from two single-port converters: a dual-band converter and a triple-band converter. The intricate design considerations for the dual-port converter are elaborated upon in the subsequent subsection.

2.2 Dual-port hexa-band converter design

The single-port dual-band and the triple-band converters are integrated to obtain a hexa-band converter comprising two input ports and a single output port. The port-1 is matched with the rectification block, incorporating an L-matching network, while port-2 is matched using a π-matching network. The schematic of the hexa-band converter is shown in Fig 11.

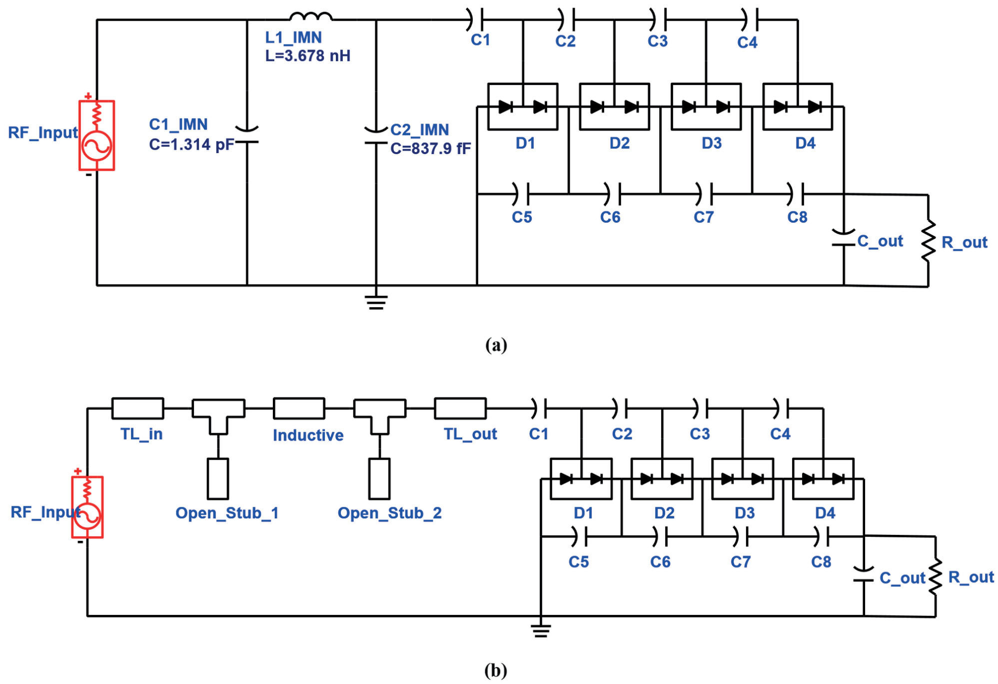

Fig 8. Schematics of RF-to-DC converters working in WiFi-2.45 GHz band utilizing: (a) Lumped π-type IMN. (b) Distributed π-type IMN.

https://doi.org/10.1371/journal.pone.0321729.g008

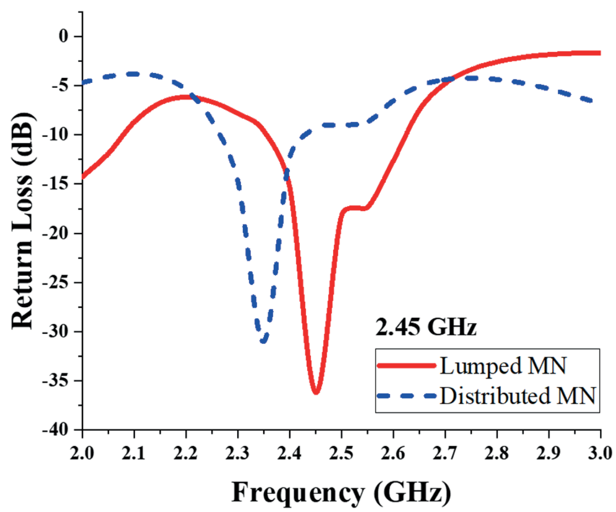

Fig 9. Return loss response of single-port single-band (2.45 GHz) Converter.

https://doi.org/10.1371/journal.pone.0321729.g009

Each of the IMN branches consists of microstrip transmission lines and open stubs, working on the required tuned frequencies. Transmission lines and stubs are interconnected by the microstrip TEEs. The layout of the IMNs and their dimensions are shown in Fig 12. All the dimensions are mentioned in millimeters (mm).

The return loss for each input port is shown in Fig 13. It can be seen that the rectifying branch-1, that is energized via port-1, provides rectification for the 870 and 1850 MHz bands

Table 4. Optimized distributed elements dimensions for triple band (1775 MHz, 2.25 GHz, and 2.45 GHz) converter.

Parameters	Dimensions $w \times l$ (mm^2)
Series inductive TL	2.4 × 14.67
Shunt open stub 1	2.4 × 5.9
Shunt open stub 2	2.35 × 10.4
Input TL section	2.36 × 5
Output TL section	2.37 × 19.95

https://doi.org/10.1371/journal.pone.0321729.t004

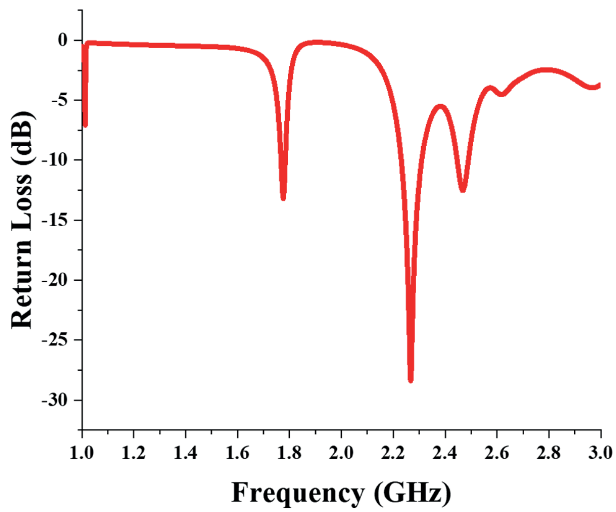

Fig 10. Return loss response of single-port triple-band (1775 MHz, 2.25 GHz, and 2.45 GHz) converter.

https://doi.org/10.1371/journal.pone.0321729.g010

and gives a dual-band response. However, rectifying branch-2, which is energized via port-2, provides a quad-band response at frequencies 1.770, 2.2, 2.4, and 2.5 GHz. The S-parameter at these frequencies is fairly below the −10 dB level.

The prototype of the converter is fabricated using an 18 $k\Omega$ output resistance and its return loss response is noticed on the virtual network analyzer (VNA). Fig 14 shows the top and bottom view of the prototype and the experimental setup established for the converter performance validation.

This research primarily involved theoretical circuit design, simulation, analysis and in-Lab testing and verification. As no field work, animal experimentation, or human subject research was conducted, therefore no specific permits were required. The research utilized commercially available software tools and readily accessible information on electromagnetic radiation and circuit components.

3 Results and discussion

The proposed converters have been simulated for different values of input power (P_{in}) and output load resistance (R_{out}). For each simulation, the corresponding values of the output DC voltage V_{out} are noticed. The output voltage is observed to increase with increasing R_{out} and P_{in}. The efficiency of the converter is given as Eq (13):

$$\eta = \frac{P_{out}}{P_{in}}, \tag{13}$$

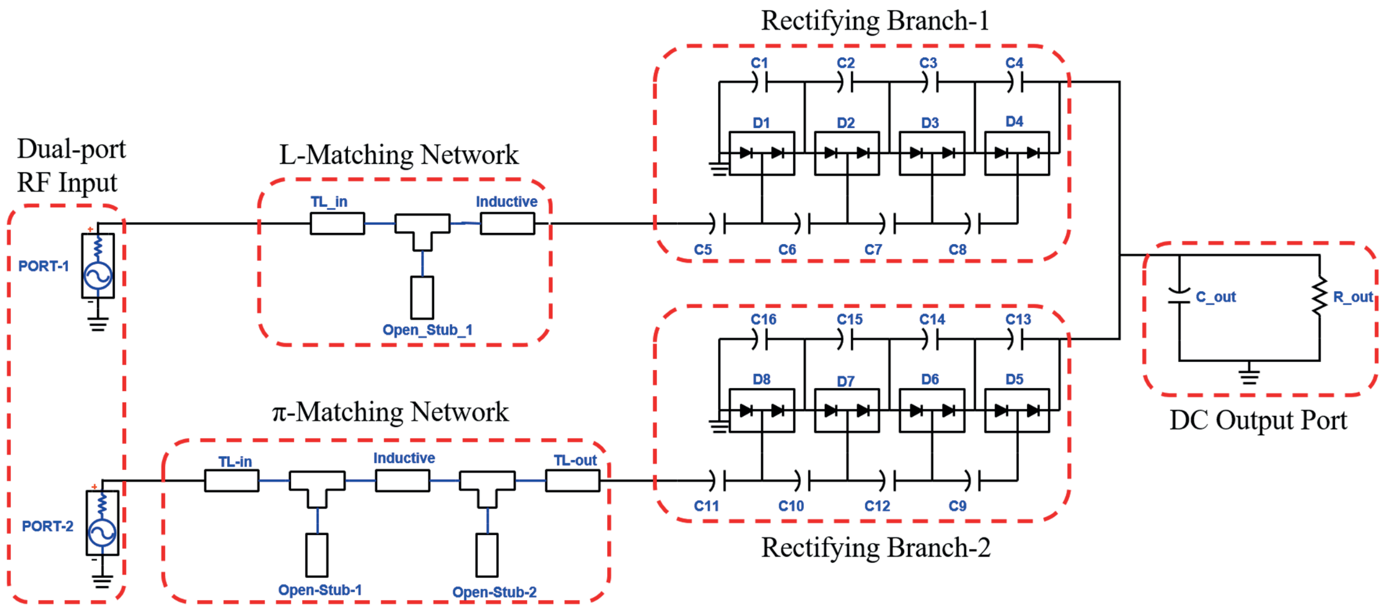

Fig 11. Hexa band converter schematic.

https://doi.org/10.1371/journal.pone.0321729.g011

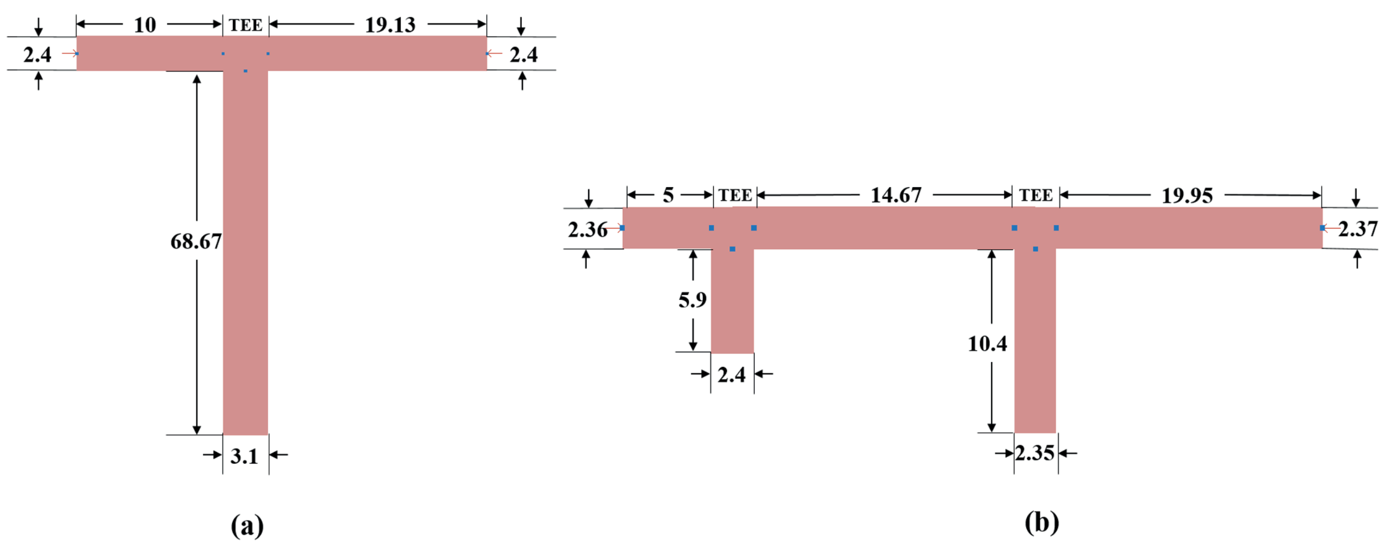

Fig 12. Proposed impedance matching networks. (a) L-type matching network. (b) π-Type matching network.

https://doi.org/10.1371/journal.pone.0321729.g012

where η is the converter efficiency, P_{out} is the output DC power and the P_{in} is the RF input power. The output DC power can be calculated as Eq (14):

$$\mathrm{P_{out}} = \frac{V_{out}^2}{R_{out}}, \tag{14}$$

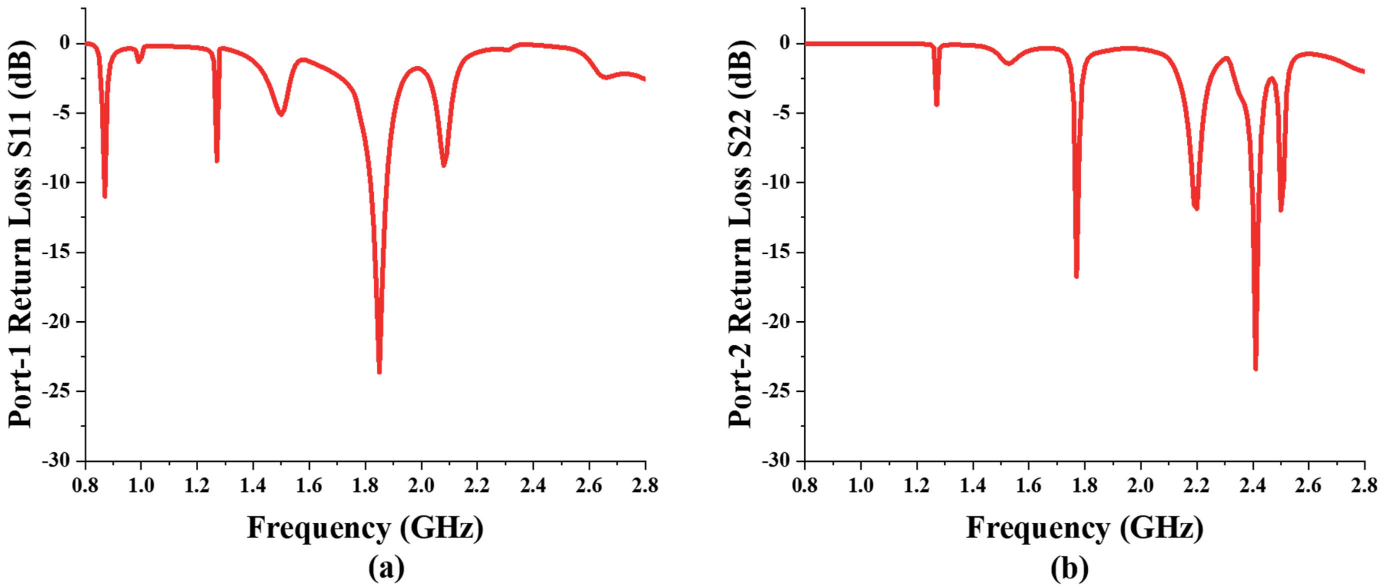

Fig 13. Return Loss for Input Ports of the Proposed converter. (**a**) Return Loss for Port-1. (**b**) Return Loss for Port-2.

https://doi.org/10.1371/journal.pone.0321729.g013

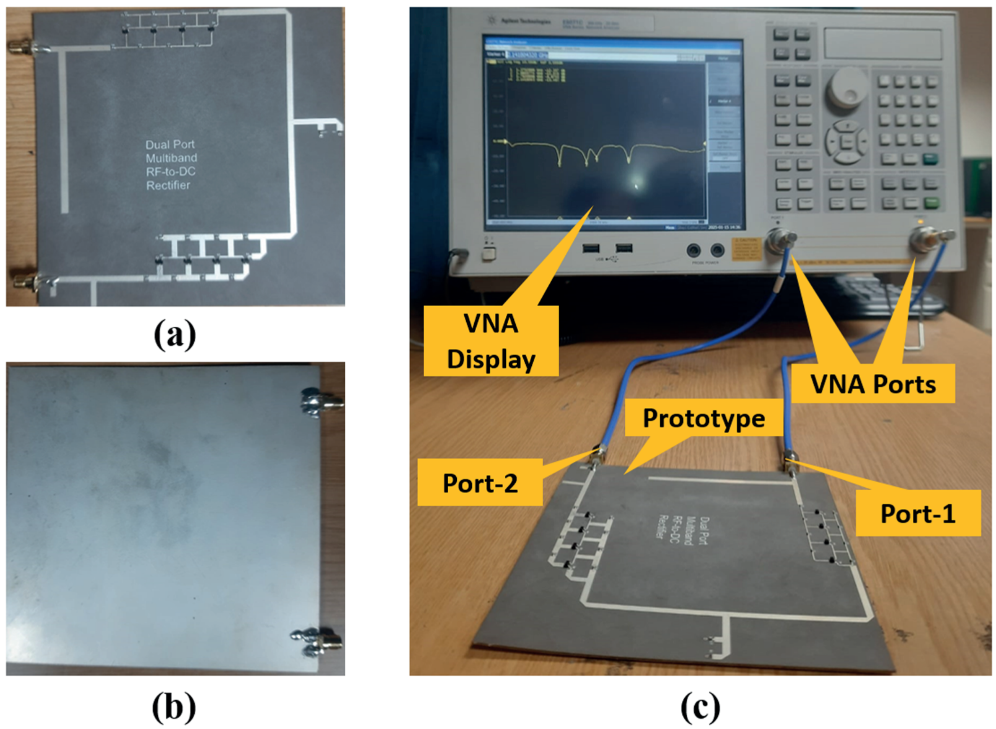

Fig 14. Prototype performance validation. (**a**) Top view. (**b**) Bottom view. (**c**) Experimental setup.

https://doi.org/10.1371/journal.pone.0321729.g014

Therefore, the efficiency η can be mentioned by the Eq (15):

$$\eta = \frac{V_{out}^2}{P_{in} \times R_{out}}, \quad (15)$$

3.1 Single port converters analysis

To determine the optimum value of the output resistance R_{out}, the efficiencies of the converters are recorded for different values of the R_{out} keeping P_{in} constant. The efficiency versus R_{out} graphs of the single-port single-band GSM-900 converter are shown in Fig 15a, using the lumped MN as well as the distributed MN. The optimum range of R_{out} is $22-26k\Omega$, and the peak efficiency of 40.3% and 42.5% is achieved with lumped MN and distributed elements MN respectively. The efficiency response of the converter against varying levels of input power Pin is shown in Fig 15b. It shows that converter gives the peak efficiency when input power is 5 dBm and output resistance is $24k\Omega$. It is also concluded that distributed matching network gives a slightly higher efficiency than lumped element matching.

Similarly, the optimum output resistance of single-port single-band 2.45 GHz converter is extracted from the analysis of its efficiency versus R_{out} graphs shown in Fig 16a. The optimum R_{out} range is $10-14k\Omega$, where the converter provides peak efficiency levels. Hence considering $12k\Omega$ as optimum R_{out}, the efficiency response of the converter against varying P_{in} levels is shown in Fig 16b. The converter peak efficiency is 41.4% when lumped components are used for matching, and 32.8% when the distributed elements are employed for matching.

The optimum output resistance for the single-port dual-band (890 MHz, and 1850 MHz) converter is extracted from its efficiency versus R_{out} graphs shown in Fig 17a. It can be seen that maximum efficiency level of about 30% is obtained when the Rout is kept 26 kΩ at –5 dbm of input power. The efficiency versus P_{in} curve is also shown in Fig 17b when Rout is kept 26 kΩ.

Likewise, to determine the optimum value of the output resistance of the single-port triple-band (1775 MHz, 2.25 GHz, and 2.45 GHz) converter, its efficiency response is noted against varying values of R_{out}, as shown in Fig 18. It shows that the converter response is appreciable

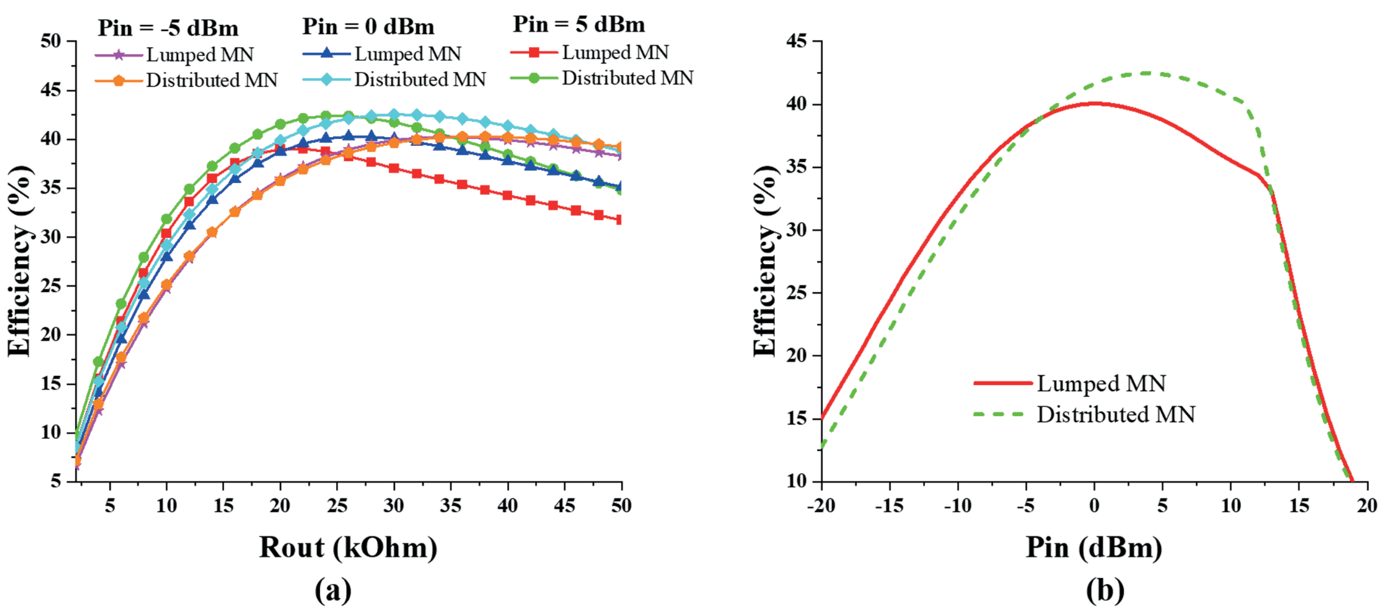

Fig 15. Single-port single-band GSM-900 converter efficiency performance against varying (a) R_{out}**. (b)** P_{in}**.**

https://doi.org/10.1371/journal.pone.0321729.g015

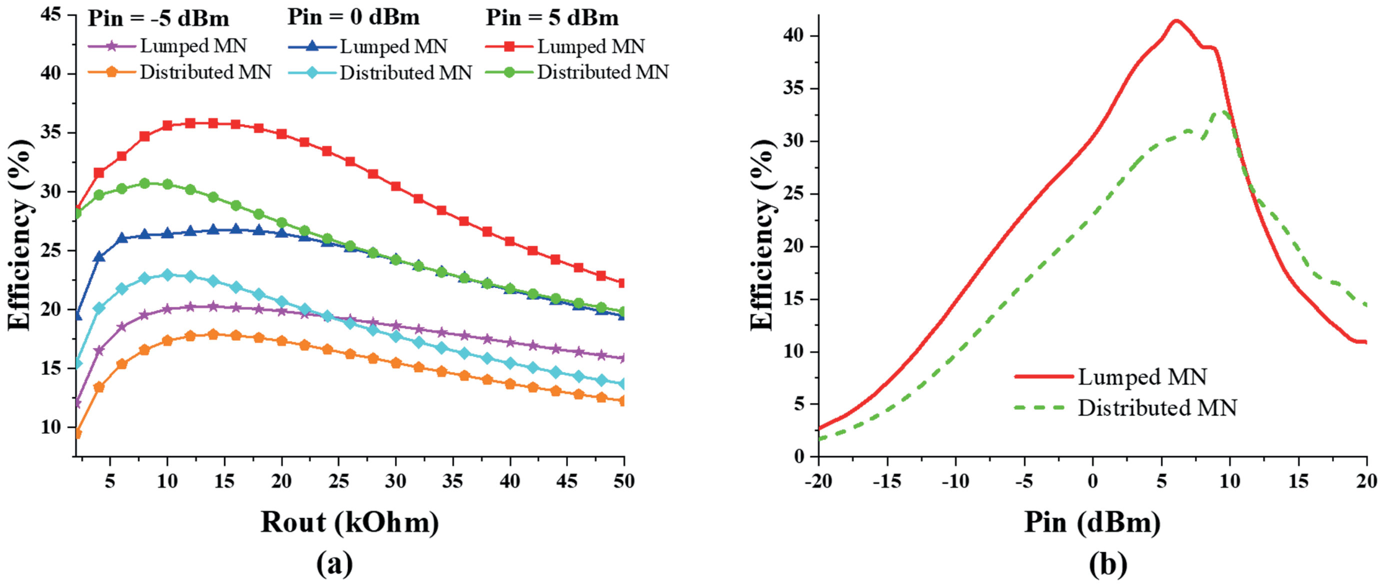

Fig 16. Single-port single-band 2.45 GHz converter efficiency performance against varying (a) R_{out}**. (b)** P_{in}**.**

https://doi.org/10.1371/journal.pone.0321729.g016

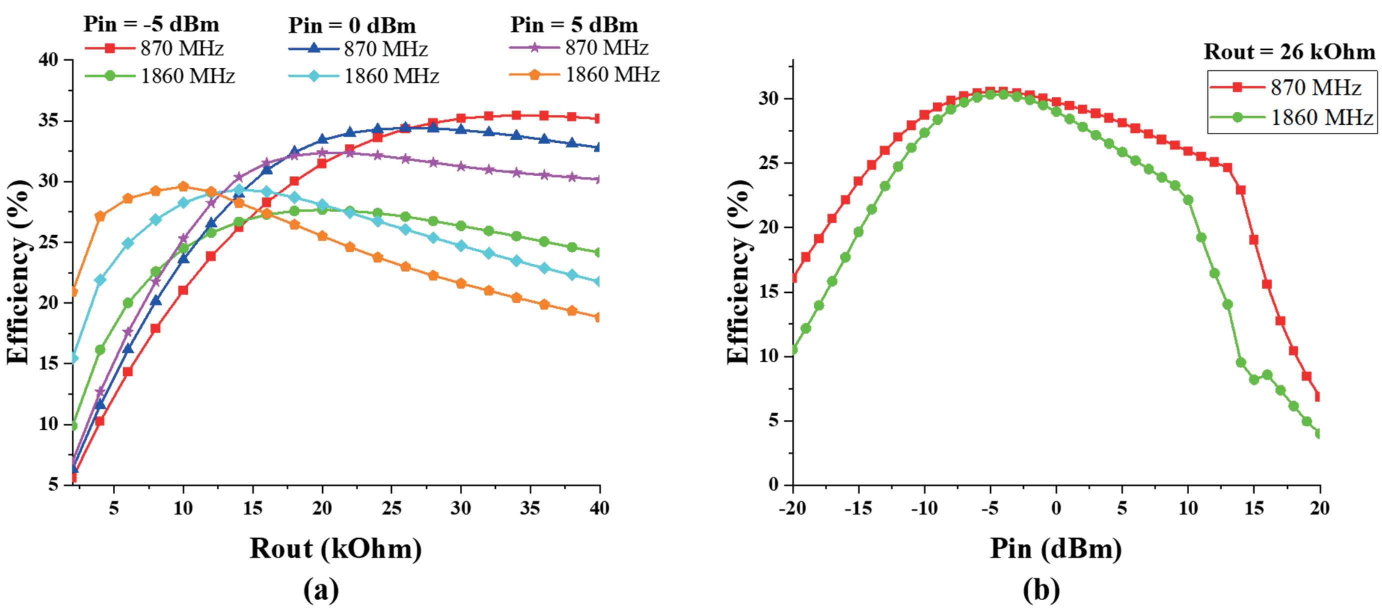

Fig 17. Single-port dual-band converter efficiency performance against varying, (a) R_{out}**. (b)** P_{in}**.**

https://doi.org/10.1371/journal.pone.0321729.g017

in the range of 10 – 15 kΩ Rout. The peak efficiency of 64% is achieved at 2.47 GHz when R_{out} is 12 kΩ and P_{in} is 10 dBm.

Fig 19 shows the efficiency response of single-port triple-band converter against varying input power, when output resistance is 10, 12 and 18 kΩ respectively. The maximum efficiency levels are recorded when the input power is in the range of 5–10 dBm.

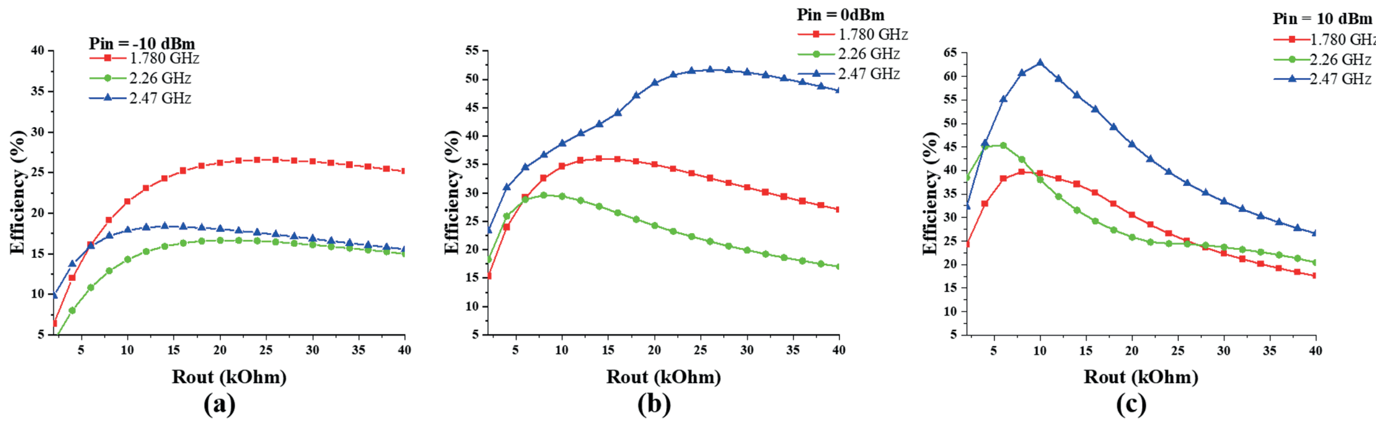

Fig 18. Single-port triple-band converter efficiency vs R_{out} curve at constant input power. (a) P_{in} = –10 dBm. (b) P_{in} = 0 dBm. (c) P_{in} = 10 dBm.

https://doi.org/10.1371/journal.pone.0321729.g018

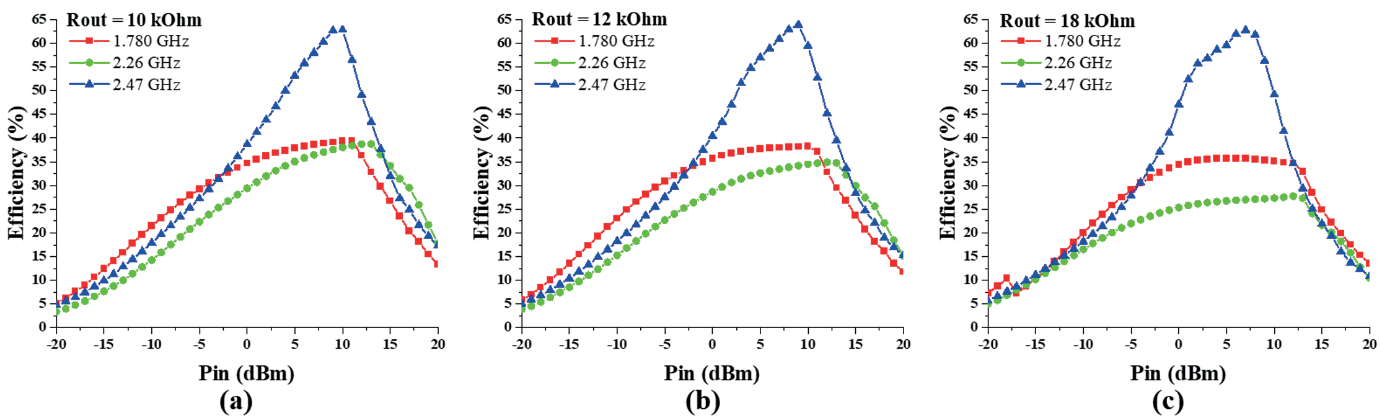

Fig 19. Single-port triple-band converter efficiency vs P_{in} curve at different R_{out} values. (a) R_{out} = 10 kΩ. (b) R_{out} = 12 kΩ. (c) R_{out} = 18 kΩ.

https://doi.org/10.1371/journal.pone.0321729.g019

3.2 Dual-port hexa-band converter analysis

The optimum value of the output resistance R_{out} for the dual-port hexa-band converter design is determined by the analysis of its efficiency response against varying R_{out}, while keeping the input power constant, as shown in Fig 20. It shows that the peak efficiencies are obtained when the output resistance value is in the range 10–20 kΩ. moreover the maximum PCE is achieved when the input power is 10 dBm (10 mW).

The efficiency vs P_{in} curve for the proposed dual-port hexa-band converter is displayed in Fig 21. It shows that the efficiency of the converter increases with the increase in input power level and attains a peak at certain value of P_{in}, after which is starts decreasing. Appreciable efficiencies are noted against 10 kΩ and 18 kΩ of output resistance.

From the analysis of the dual-port hexa-band converter responses against varying P_{in} levels and varying values of R_{out}, it can be seen that the converter attains peak efficiency levels of 66% and 62% for 10 kΩ and 18 kΩ output resistance, respectively. The converter peak efficiency responses are summarized in Table 5.

The proposed design is compared with some recent RF-to-DC converter designs presented in the literature to highlight significance of the proposed converter. The comparison is summarized in Table 6. It can be seen that the proposed converter has achieved hexa-band

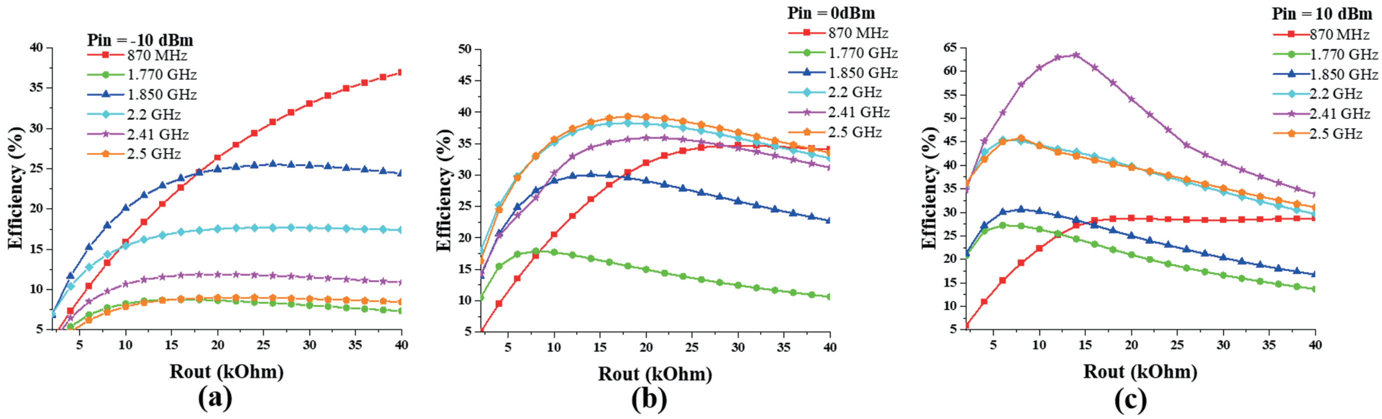

Fig 20. hexa band converter efficiency vs R_{out} curve at constant input power. (**a**) P_{in} = −10 dBm. (**b**) P_{in} = 0 dBm. (**c**) P_{in} = 10 dBm.

https://doi.org/10.1371/journal.pone.0321729.g020

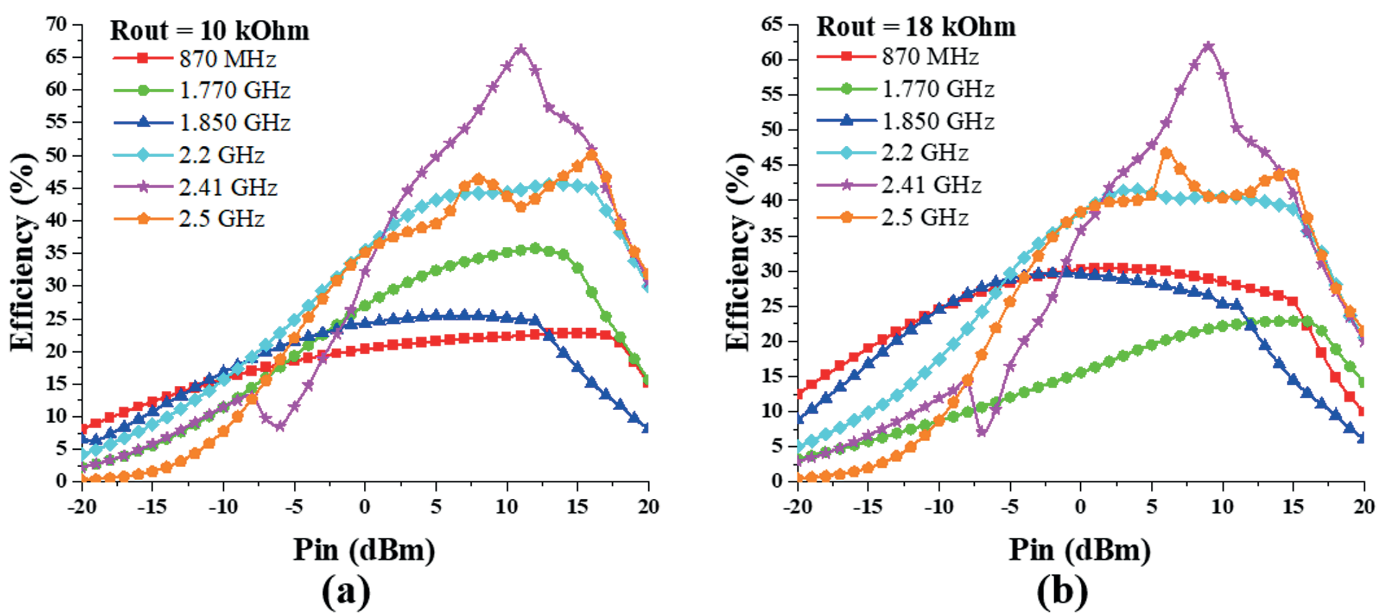

Fig 21. Hexa band converter efficiency vs P_{in} curve at different rout values. (a) R_{out} = 10 kΩ. (b) R_{out} = 18 kΩ.

https://doi.org/10.1371/journal.pone.0321729.g021

Table 5. Summarized dual-port hexa-band converter peak efficiency performance.

Rout	10 (kΩ)			18 (kΩ)		
Frequency	η (%)	V_{out} (V)	P_{in} (dBm)	η (%)	V_{out} (V)	P_{in} (dBm)
870 MHz	22.7	4.49	15	30.2	2.33	0
1770 MHz	35.5	6.69	11	23	11.41	15
1850 MHz	25.5	3.5	6	29.7	2.1	−1
2.2 GHz	45.5	10.7	14	41.5	4.33	4
2.41 GHz	66	9.13	11	62	9.4	9
2.5 GHz	46.4	5.41	8	46.7	5.8	6

https://doi.org/10.1371/journal.pone.0321729.t005

Table 6. Comparison of proposed converter with some other designs in literature.

Ref.	Band (GHz)	η (%)	P_{in} (dBm)	R_{out} (kΩ)	V_{out} (V)
[16]	0.900	29.85	20		17.58
[35]	2.5	33.5	5		1.89
[20]	1.8	41	0	30	
	2.45	20			
[8]	0.900	33.7	−10	3.8	0.02–3.8
	1.8	21.8			
	2.45	20			
[36]	0.89	60			0.19–12.43
	1.83	48			
	2.19	35			
	2.45	25			
[27]	0.55	–		10–75	
	0.75	–			
	0.9	67			
	1.85	–			
	2.15	–			
	2.45	–			
[28]	1.84	44.4	−10		
	2.04	43.9			
	2.36	45.4			
	2.54	43.4			
	3.3	36.1			
	4.76	32.4			
	5.8	28.3			
Proposed work with 10 kΩ R_{out}	0.87	22	10	10	5.3–9.13
	1.770	35			
	1.850	25			
	2.2	44.5			
	2.41	63.6			
	2.5	44			
Proposed work with 18 kΩ R_{out}	0.87	29	9	18	2.1–11.4
	1.770	22			
	1.850	26.5			
	2.2	40.6			
	2.41	62			
	2.5	40.6			

https://doi.org/10.1371/journal.pone.0321729.t006

rectification with comparable PCE levels. The proposed design's performance outshines in terms of its multiband PCE by achieving simultaneous impedance matching in diverse frequency bands of the two port converter.

4 Conclusion

This article explores a Dual-Port Multiband RF-to-DC converter designed to meet dynamic energy needs of IoT devices. The innovative design on a 0.78 mm thick Rogers-5880 substrate demonstrates adaptability for diverse IoT environments. By harnessing RF energy from 870 MHz, 1770 MHz, 1850 MHz, 2.2 GHz, 2.4 GHz and 2.5 GHz bands simultaneously, it significantly boosts energy acquisition. The proposed circuitry and impedance matching techniques are used to optimize conversion efficiency and output voltage across all the desired RF frequencies, simultaneously. Systematic analysis of parameters like output voltage and conversion efficiency provides valuable performance insights. The impressive efficiency figures are observed across different frequency bands (0.87–2.5 GHz) for 10 kΩ as well as 18 kΩ output resistance. The proposed design exhibits peak efficiency of 66% and 62% at 10 kΩ and 18 kΩ, respectively. Comparative analysis with recent converter designs highlights its multiband capability, impressive efficiency, innovative impedance matching techniques, competitiveness and innovation for energy-efficient IoT solutions. This work holds great promise for practical implementation in various IoT environments, ultimately facilitating the growth of sustainable and autonomous IoT ecosystems.

Acknowledgments

This work was supported by Researchers Supporting Project number (RSP2025R474), King Saud University, Riyadh, Saudi Arabia.

Author contributions

Conceptualization: Bismah Tariq, Muhammad Amjad, Waqar Ahmad Malik.

Data curation: Bismah Tariq, Waqar Ahmad Malik.

Formal analysis: Bismah Tariq, Waqar Ahmad Malik.

Funding acquisition: Khaled A. Al-Jaloud, Rifaqat Hussain.

Investigation: Bismah Tariq, Syed Tamoor Shah.

Methodology: Bismah Tariq, Waqar Ahmad Malik.

Project administration: Muhammad Amjad, Khaled A. Al-Jaloud, Syed Tamoor Shah.

Resources: Rifaqat Hussain.

Software: Bismah Tariq, Waqar Ahmad Malik.

Supervision: Muhammad Amjad.

Validation: Bismah Tariq, Waqar Ahmad Malik.

Visualization: Bismah Tariq, Waqar Ahmad Malik.

Writing – original draft: Bismah Tariq.

Writing – review & editing: Bismah Tariq, Muhammad Amjad, Waqar Ahmad Malik.

References

1. Woo J, Shin S, Asutosh AT, Li J, Kibert CJ. An overview of state-of-the-art technologies for data-driven construction. In: Proceedings of the 18th International Conference on Computing in Civil and Building Engineering: ICCCBE 2020. Springer; 2021. pp. 1323–34.
2. Dorri A, Kanhere SS, Jurdak R, Gauravaram P. Blockchain for IoT security and privacy: The case study of a smart home. In: 2017 IEEE International Conference on Pervasive Computing and Communications Workshops (PerCom Workshops). IEEE; 2017. pp. 618–23.
3. Wagih M, Weddell AS, Beeby S. Rectennas for radio-frequency energy harvesting and wireless power transfer: a review of antenna design [antenna applications corner]. IEEE Antennas Propag Mag. 2020;62(5):95–107. http://dx.doi.org/10.1109/MAP.2020.3012872
4. Bougas ID, Papadopoulou MS, Boursianis AD, Kokkinidis K, Goudos SK. State-of-the-art techniques in RF energy harvesting circuits. Telecom. MDPI; 2021;2;369–89. http://dx.doi.org/10.3390/telecom2040022
5. Pandey R, Shankhwar AK, Singh A. Design and analysis of rectenna at 2.42 GHz for Wi-Fi energy harvesting. Progress Electromagn Res C. 2021;117:89–98. http://dx.doi.org/10.2528/PIERC21100409
6. Chen Z, Law MK, Mak PI, Martins RP. A single-chip solar energy harvesting IC using integrated photodiodes for biomedical implant applications. IEEE Trans Biomed Circuits Syst. 2016;11(1):44–53. http://dx.doi.org/10.1109/TBCAS.2016.2553152

7. Hosain MK, Kouzani AZ, Samad MF, Tye SJ. A miniature energy harvesting rectenna for operating a head-mountable deep brain stimulation device. IEEE Access. 2015;3:223–34. http://dx.doi.org/10.1109/ACCESS.2015.2414411
8. Khan NU, Khan FU. RF energy harvesting for portable biomedical devices. In: 22nd International Multitopic Conference (INMIC). IEEE; 2019. pp. 1–6.
9. Zhang C, Du H, Ge J. Energy-efficient power allocation in energy harvesting two-way AF relay systems. IEEE Access. 2017;5:3640–5. http://dx.doi.org/10.1109/ACCESS.2017.2670641
10. Zhang H, Guo Yx, Zhong Z, Wu W. Cooperative integration of RF energy harvesting and dedicated WPT for wireless sensor networks. IEEE Microw Wirel Compon Lett. 2019;29(4):291–3. http://dx.doi.org/10.1109/LMWC.2019.2902047.
11. Shafique K, Khawaja BA, Khurram MD, Sibtain SM, Siddiqui Y, Mustaqim M, et al. Energy harvesting using a low-cost rectenna for Internet of Things (IoT) applications. IEEE Access. 2018;6:30932–41. http://dx.doi.org/10.1109/ACCESS.2018.2834392
12. Awais Q, Jin Y, Chattha HT, Jamil M, Qiang H, Khawaja BA. A compact rectenna system with high conversion efficiency for wireless energy harvesting. IEEE Access, 2018;6:35857–66. http://dx.doi.org/10.1109/ACCESS.2018.2848907
13. Tafekirt H, Pelegri-Sebastia J, Bouajaj A, Reda BM. A sensitive triple-band rectifier for energy harvesting applications. IEEE Access. 2020;8:73659–64. http://dx.doi.org/10.1109/ACCESS.2020.2986797
14. Kim S, Vyas R, Bito J, Niotaki K, Collado A, Georgiadis A, et al. Ambient RF energy-harvesting technologies for self-sustainable standalone wireless sensor platforms. Proc IEEE. 2014;102(11):1649–66. http://dx.doi.org/10.1109/JPROC.2014.2357031
15. Lee YC, Ramiah H, Choo A, Churchill KKP, Lai NS, Lim CC, et al. High-performance multiband ambient RF energy harvesting front-end system for sustainable IoT applications—a review. IEEE Access. 2023;11:11143–64. http://dx.doi.org/10.1109/ACCESS.2023.3241458
16. Ali EM, Yahaya NZ, Saraereh OA, Assaf AHA, Alqasem BH, Iqbal S, et al. Power conversion using analytical model of Cockcroft–Walton voltage multiplier rectenna. Electronics. 2021;10(8):881. http://dx.doi.org/10.3390/electronics10080881
17. Selim KK, Wu S, Saleeb DA. An optimized rectifier design for RF energy harvesting at the 2.45 GHz WiFi frequency band. In: 27th International Conference on Telecommunications (ICT). IEEE; 2020. pp. 1–5.
18. Bougas ID, Papadopoulou MS, Boursianis AD, Sarigiannidis P, Nikolaidis S, Goudos SK. Rectifier circuit design for 5G energy harvesting applications. In: 11th International Conference on Modern Circuits and Systems Technologies (MOCAST). IEEE; 2022. pp. 1–4.
19. Khansalee E, Zhao Y, Leelarasmee E, Nuanyai K. A dual-band rectifier for RF energy harvesting systems. In: 11th International Conference on Electrical Engineering/Electronics, Computer, Telecommunications and Information Technology (ECTI-CON). IEEE; 2014. pp. 1–4.
20. Abdl-Ghany OM, Sobih AG, El-Tager AM. Improved RF energy harvesting rectifier targeting ambient local sources of DTV, cellular networks and Wi-Fi. In: 13th International Conference on Electrical Engineering (ICEENG). IEEE; 2022. pp. 100–4.
21. Muhammad S, Tiang JJ, Wong SK, Smida A, Ghayoula R, Iqbal A. A dual-band ambient energy harvesting rectenna design for wireless power communications. IEEE Access. 2021;9:99944–53. http://dx.doi.org/10.1109/ACCESS.2021.3096834
22. Sarma SS, Chandravanshi S, Akhtar MJ. Triple band differential rectifier for RF energy harvesting applications. Asia-Pacific Microwave Conference (APMC). New Delhi, India, 2016, pp. 1–4. http://dx.doi.org/10.1109/APMC.2016.7931295.
23. Shen S, Chiu CY, Murch RD. A dual-port triple-band L-probe microstrip patch rectenna for ambient RF energy harvesting. IEEE Antennas Wireless Propag Lett. 2017;16:3071–4. http://dx.doi.org/10.1109/LAWP.2017.2761397
24. Skaik T. A quad-band rectifier design with improved matching bandwidth for RF energy harvesting applications. In: 2017 International Conference on Promising Electronic Technologies (ICPET), Deir El-Balah, Palestine, 2017, pp. 82–86. http://dx.doi.org/10.1109/ICPET.2017.21
25. Vu HS, Nguyen N, Ha-Van N, Seo C, Le MT. Multiband ambient RF energy harvesting for autonomous IoT devices. IEEE Microw Compon Lett. 2020;30(12):1189–92. http://dx.doi.org/10.1109/LMWC.2020.3029869
26. Muhammad S, Tiang JJ, Wong SK, Smida A, Waly MI, Iqbal A. Efficient quad-band RF energy harvesting rectifier for wireless power communications. AEU-Int J Electron Commun. 2021;139:153927. https://doi.org/10.1016/j.aeue.2021.153927
27. Song C, Huang Y, Carter P, Zhou J, Yuan S, Xu Q, et al. A novel six-band dual CP rectenna using improved impedance matching technique for ambient RF energy harvesting. IEEE Trans Antennas Propag. 2016;64(7):3160–71. https://doi.org/10.1109/TAP.2016.2565697

28. Wang Y, Zhang J, Su Y, Jiang X, Zhang C, Wang L, et al. Efficiency enhanced seven-band omnidirectional rectenna for RF energy harvesting. IEEE Trans Antennas Propag. 2022;70(9):8473–84. https://doi.org/10.1109/TAP.2022.3177492

29. Mansour MM, Kanaya H. Compact and broadband RF rectifier with 1.5 octave bandwidth based on a simple pair of L-section matching network. IEEE Microw Compon Lett. 2018;28(4):335–7. https://doi.org/10.1109/LMWC.2018.2808419

30. Liu W, Huang K, Wang T, Zhang Z, Hou J. A broadband high-efficiency RF rectifier for ambient RF energy harvesting. IEEE Microw Compon Lett. 2020;30(12):1185–8. https://doi.org/10.1109/LMWC.2020.3028607

31. Wang X, Jin B, Huang L, Zhang M, Fang M. A novel high-sensitivity broadband rectifier for ambient RF energy harvesting. Radioengineering. 2022;31(3):331. http://dx.doi.org/10.13164/re.2022.0331

32. Rani N, Kaur J, Bhatia H, Saini SS, Kaur R, Sidhu E. Design and performance analysis of Cockroft-Walton Voltage Multiplier (CWVM) energy harvesting for low power applications. In: 2017 Progress in electromagnetics research symposium - Spring (PIERS), St. Petersburg, Russia, 2017, pp. 2131–6. http://dx.doi.org/10.1109/PIERS.2017.8262103

33. Balanis CA. Advanced engineering electromagnetics. John Wiley & Sons; 2012.

34. Balanis CA. Antenna theory: analysis and design. John Wiley & Sons; 2016.

35. Sharma, Priya, Ashutosh Singh, B. Naresh, and Vinod Singh. A novel rectenna design: To make Wireless Sensor Network Technology Affordable for Low-Income Countries. 2022. http://dx.doi.org/10.21203/rs.3.rs-1913574/v1

36. Roy S, Tiang JJ, Roslee MB, Ahmed MT, Kouzani AZ, Mahmud MP. Quad-band rectenna for ambient radio frequency (RF) energy harvesting. Sensors (Basel). 2021;21(23):7838. doi: 10.3390/s21237838 PMID: 34883846